

Single crystal studies and electronic structure investigation of a room temperature semiconductor NaMnAs

Jiří Volný

*Department of Condensed Matter Physics, Faculty of Mathematics and Physics,
Charles University, Ke Karlovu 5, Praha 2, CZ-12116*

Václav Holý

*Department of Condensed Matter Physics, Faculty of Mathematics and Physics,
Charles University, Ke Karlovu 5, Praha 2, CZ-12116 and
Institute of Condensed Matter Physics, Faculty of Science,
Masaryk University, Kotlářská 2, Brno, CZ-61137*

Kateřina Charvátová, Martin Veis

*Department of Condensed Matter Physics, Faculty of Mathematics and Physics,
Charles University, Ke Karlovu 5, Praha 2, CZ-12116*

M. Vondráček, J. Honolka

FZU - Institute of Physics of the Czech Academy of Sciences, Na Slovance 2, Praha 8, CZ-18221

Elen Duverger-Nédellec

*Department of Condensed Matter Physics, Faculty of Mathematics and Physics,
Charles University, Ke Karlovu 5, Praha 2, CZ-12116 and
CNRS, ICMCB UMR5026, Bordeaux INP, University of Bordeaux, Pessac, F-33600*

J. Schusser*

New Technologies-Research Center, University of West Bohemia, Plzeň 3, CZ-30100

S.W. D'Souza, J. Minár

New Technologies-Research Center, University of West Bohemia, Plzeň 3, CZ-30100

James M. Pientka

Department of Physics, St. Bonaventure University, St. Bonaventure, NY-14778

Alberto Marmodoro, Karel Výborný

Institute of Physics, Academy of Science of the Czech Republic, Cukrovarnická 10, Praha 6, CZ-16253

Klára Uhlířová

*Department of Condensed Matter Physics, Faculty of Mathematics and Physics,
Charles University, Ke Karlovu 5, Praha, CZ-12116[†]*

(Dated: Sep07, 2021)

We report synthesis of single crystalline NaMnAs, confirm its antiferromagnetic order and characterise the sample by photoemission spectroscopy. The electronic structure was studied using optical transmittance, x-ray and ultraviolet spectroscopy and by theoretical modeling using local density approximation (LDA) extended to LDA+U when Heisenberg model parameters were determined. Optical transmittance measurement have confirmed the theoretical predictions that NaMnAs is a semiconductor. Also the Néel temperature was closer determined for the first time from temperature dependence of magnetization, in agreement with our Monte Carlo simulations.

I. INTRODUCTION

Antiferromagnets (AFMs) are increasingly coming into the spotlight for spintronics applications [1–4]. One

of the motivations is robustness against stray magnetic fields for memory devices applications [5–7], thanks to compensation of magnetic moments. The aspect of linear spin waves dispersion close to the Γ point, as opposed to the quadratic trend in ferromagnets [8], has also been considered for possible magnonics technology [8–14].

While numerous AFM materials were discovered in previous century, for many of them, little is known beyond the bare fact that they are antiferromagnetic. One

* Experimentelle Physik VII and Würzburg-Dresden Cluster of Excellence ct.qmat, Universität Würzburg, Würzburg, D-97074

[†] klara@mag.mff.cuni.cz

of the most widely studied compounds in AFM spintronics [15, 16], CuMnAs shows switching behavior in charge resistivity between binary [17] or multi-level [6] states, through the controlled application of electric current [18, 19] or optical [20] pulses. Its tetragonal phase presents the additional benefits of above room temperature antiferromagnetic ordering [21–26], as well as lack of lattice strain in the deposition over a GaP substrate.

On the other hand, similarly to the other well-established example of Mn₂Au, CuMnAs presents no electronic band gap [27]. This feature would be highly desirable for further spintronics and magnonics technologies, in which for instance lack of charge carriers have been predicted [28] and observed [29, 30] to provide long range magnons diffusion length due to the depopulated Stoner continuum.

While the pursuit of better characterization of microscopic features and switching mechanisms in the most established AFMs continues, and typically resorts to high quality samples prepared by molecular beam epitaxy (MBE) [31–33], the search for other semiconducting AFMs has also carried on, taking advantage of the flexibility offered by bulk synthesis methods in exploring different compositions and lattice geometries.

Remaining within the AMnX family of alkaline metal / manganese-pnictide ternary compounds with a tetragonal non-symmorphic space group P4/nmm (Cu₂Sb-type structure), we recall the early work by Linowsky and Bronger (with $A = \text{K}$ and $X = \text{P, As}$) [34] Schuster et al. (with $A = \text{K, Na}$ and $X = \text{Sb, Bi, P}$) [35], Achenbach et al. (with $A = \text{Li, Na}$ and $X = \text{P, As, Sb, Bi}$) [36], Bronger et al. ($X = \text{Na, Li, K}$ and $X = \text{P, As, Sb, Bi}$) [37]. The later work showed that all these compound order antiferromagnetically well above the room temperature. These materials have recently been rediscovered as potential antiferromagnetic semiconductors [31, 38–42]. Here, we would like to focus on NaMnAs. Up to now only the crystal structure and magnetic structure by XRD and neutron diffraction, respectively, was reported on pulverised polycrystals [2,6]. It has been shown that it orders antiferromagnetically with magnetic moments aligned along z -axis and propagation vector $k = [000]$. The Néel temperature was estimated between 293 and 643 K; close to zero temperature, the Mn-magnetic moment was determined to be $4.0 \mu_B/\text{Mn}$ [37].

We report on the high quality single crystal growth of NaMnAs, confirm by optical transmission measurements its semiconducting nature and discuss various aspects of magnetic order both from experimental and theoretical point of view.

II. SAMPLE GROWTH AND CHARACTERIZATION

The NaMnAs single crystals were grown similar to Cu_{1-x}Mn_{1+x}As using the flux method [43]. The single crystals were shiny flat rectangular plates ($2 \times 2 \times$

0.1 mm³), which can be cleaved in the basal plane using a standard sticky tape. This suggests very weak bonds between the layers. A typical sample is shown in Fig. 2. The material is not stable on air. After few minutes it becomes dark so most of the manipulation has to be done under protective atmosphere (see Supplemental Material). It is rather typical for the flux method, that also other phases are grown; in this case MnAs crystals were formed during the synthesis. They form tiny needles which are often attached to the surface of NaMnAs crystals and are difficult to remove. This does not affect any spectroscopic measurements which are performed on impurity-free, cleaved surfaces. They influence however other bulk measurements such as magnetization (as discussed later).

A. Composition and crystal quality

The composition and the crystal structure of selected single crystals have been determined by energy-dispersive x-ray spectroscopy (EDS) and by single-crystal x-ray diffraction (XRD), respectively. EDS was performed using Scanning Electron Microscope (SEM) equipped with an energy dispersive x-ray detector Bruker AXS which utilizes ESPRIT software package (a non-standard method with precision up to 1 %). The as-grown samples were mounted on a SEM stub using carbon tape, freshly cleaved, and quickly installed into the SEM. The surfaces appear very flat and homogeneous with the stoichiometry: Na_{0.96(0.02)}Mn_{1.07(0.02)}As_{0.97(0.02)}, reproducible across several growth-batches. High resolution XRD using Rigaku Smartlab 45/200 in parallel beam mode was performed on an as grown single crystal with the (001) planes parallel to the sample holder. The sample was preserved by kapton tape during the measurement. From the refined XRD peaks positions, a Cohen-Wagner plot provides the lattice parameters: $a = b = 4.213 \pm 0.002$ and $c = 7.0955 \pm 0.0005$ (Å). The higher precision of the c -parameter is due to the higher number of measured (001) diffraction peaks. Also the free z -component of the 2c atomic position was refined being 0.6675 and 0.2166 for Na and As atoms, respectively. The standard single crystal diffraction collecting the full diffraction pattern was performed as well, however, the crystals exhibit large degree of mosaicity, preventing proper crystal structure refinement (See Supplemental Material at).

Fig. 1 shows a symmetric $2\theta/\omega$ scan of the (001) diffraction peaks. The peak width is limited by the resolution of the diffractometer, and it suggests excellent homogeneity of the crystals. Additionally, scans across the (205) and (206) directions were performed in order to determine the a lattice parameter.

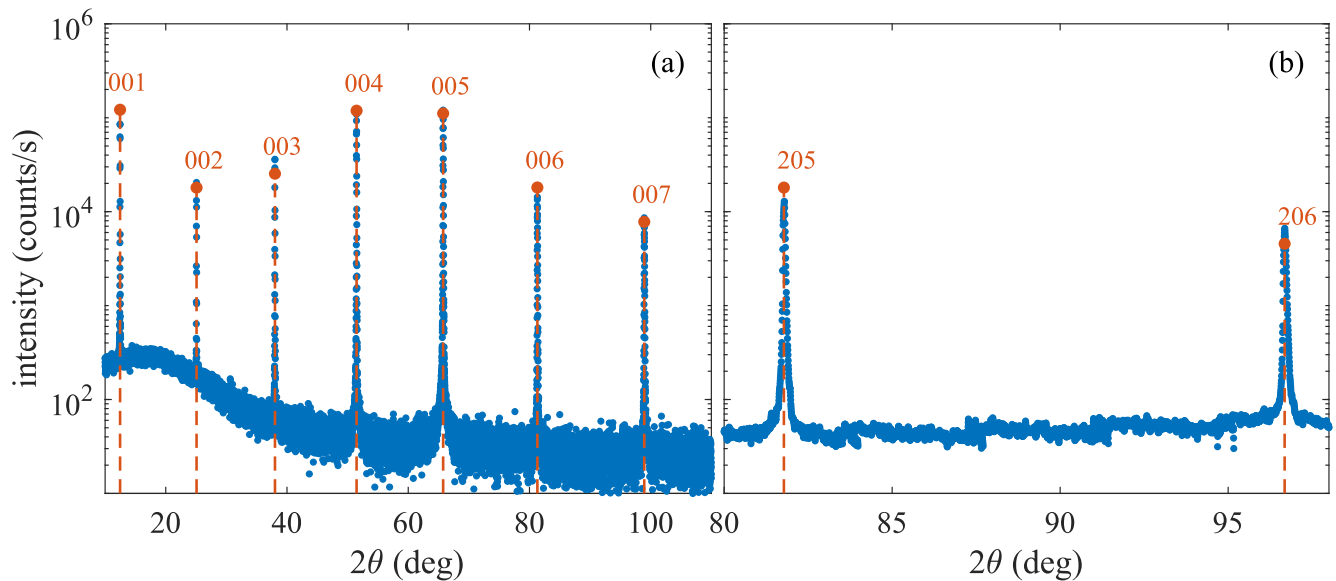


FIG. 1. Symmetric $2\theta/\omega$ scan of the (001) NaMnAs single crystals (a), and Q_z scan across the (205) and (206) directions, a and (b), respectively. Open circles represent the calculated diffraction intensities, using the crystal structure from Ref. [37]. In the calculation we assumed an ideal kinematically diffracting crystal lattice

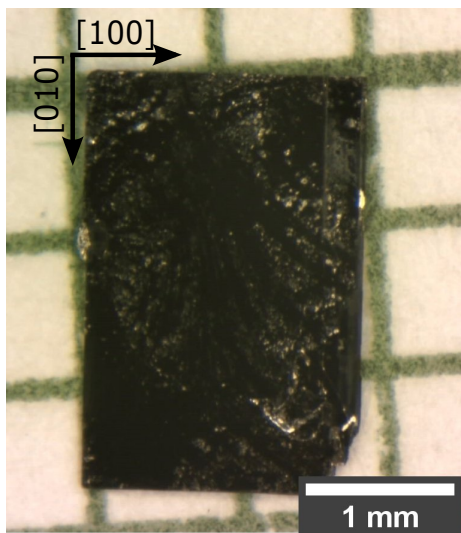


FIG. 2. Optical microscope image of typical NaMnAs single crystal. The sample thickness is in the order of $100 \mu\text{m}$. The c -axis is pointing perpendicular to the plane while a -axes are parallel with the long edges of the sample.

B. X-ray photoemission spectroscopy

The sample was investigated by x-ray photoemission spectroscopy (XPS) after a fresh cleave under UHV conditions. Sodium, arsenic and manganese shallow core levels (CLs) were probed using monochromatised Al $K\alpha$ radiation ($\hbar\omega = 1486.7 \text{ eV}$), revealing depth-sensitive information about the sample composition and its homo-

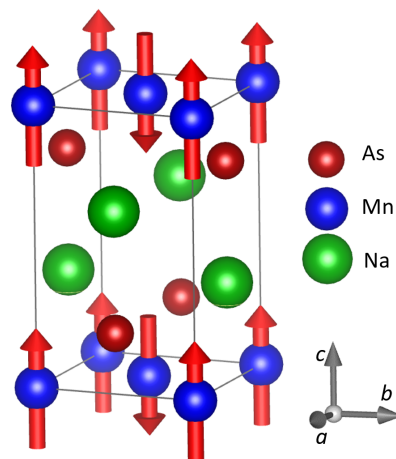


FIG. 3. Unit cell of NaMnAs with magnetic moment directions refined by Bronger et al. [37].

geneity as discussed in the Supplemental Material. In addition, details in the spectral lineshape of Mn CLs allows an insight into the Mn $3d$ shell configuration. The Mn $2p$ CL in Fig. 4 shows a complex spectral shape, which can be reproduced using six fitted Voigt profiles (referred to as P1–P6) and a ranged Shirley background. Energy positions, widths, and intensities of the Voigt profiles are summarised in Tab. I. The double-peak structure (P1 and P2 separated by 1.1 eV in our case) of the $2p_{3/2}$ CL is a typical multiplet splitting effect in Mn observed for example in bulk Mn-oxides with Mn^{2+} or Mn^{3+} and even Mn^{4+} states due to strong crystal field effects.[44]

	P_1	P_2	P_3	P_4	P_5	P_6
Energy [eV]	639.33	640.38	641.70	643.46	650.73	651.42
FWHM [eV]	0.75	1.41	0.97	4.05	1.06	1.60
Area [a.u.]	169	260	37	114	65	89

TABLE I. Peak energy positions, FWHM values, and total intensities of Voigt peaks $P_1 - P_6$ in Fig.4. For $P_1 - P_3$ and $P_5 - P_6$ natural linewidths of 0.3 eV and 0.9 eV were assumed, respectively.

However, such a double-peak structure has also been observed [45] for single Mn atoms embedded in Bi_2Te_3 , where peaks can be reproduced in a MnX_6 (e.g. $X = \text{Br}$) cluster model[46] with Mn in a 2+ state. Splitting effects in the $2p_{1/2}$ CL (P_5 and P_6) are similar[45, 46] but broadened due to super-Coster-Kronig decay processes, which limits the information on the Mn chemical state. Finally, the smaller spectral feature P_3 located at 1.3 eV higher binding energy (BE) compared to P_2 may belong to a $J = 1, 2, 3, 4$ series of bound states between $2p_{3/2}$ hole and $3d$ valence electrons[47].

In the following we will discuss possible charge-transfer (CT) effects, which have been identified e.g. in MnO spectra[48]. Despite the convincingly present feature P_4 (we were unable to obtain good fits when P_4 is removed), we believe that a CT peak is absent. This feature found in Fig. 5 of Ref. 48 is located at significantly higher energies than P_4 in our measurements. On the other hand, shake-up satellite of the $2p_{3/2}$ CL was reported at lower energies [49]. The absence of the CT peak bears witness against ionic character of binding in our samples, consistent with ab initio predictions discussed later. We therefore conclude that the object of our study has grown in the desired composition (without significant amounts of other phases such as MnAs or manganese oxides) and relegate a more detailed analysis of the XPS for later investigations.

C. Ultraviolet photoemission spectroscopy

The same device (as in the case of XPS) with a different photon excitation energy ($\hbar\omega = 21.2$ eV, He I line) was used to obtain UPS data shown in Fig.5 covering BEs in the range [2 eV, -0.5 eV] measured in normal emission at a photon energy of 21.2 eV. The reference point $E = 0$ eV corresponds to the Fermi level of the PES analyzer. In semiconductors the position of the Fermi energy (E_F) with respect to the valence band maximum (VBM) is sensitive to defect states and possible surface band bending effects. Kraut *et al.*[50] described procedures to quantify defect induced shifts in E_F and band bending in the semiconductor GaAs by referencing shallow CLs such as $E_{\text{Ga } 3d}$ to the VBM value E_{VBM} . Thereby values E_{VBM} are estimated using the leading edge method, which approximates the density of states (DOS) by a tangential line at the maximum steepness of the VB edge.

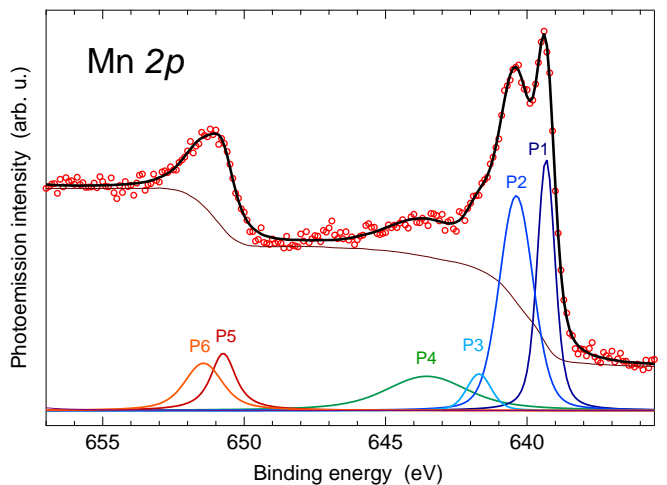


FIG. 4. XPS of the Mn $2p$ core level. Peaks and the fitting procedure are discussed in the text, the broad peak P_4 is the shake-up feature.

In our case the tangential line of the dominant intensity suggests a VBM at $E = 0.19$ eV. Looking more closely to the UPS intensity at lower BEs (see inset in Fig.5), it is evident that the intensity stretches all the way to $E = 0$ and then disappears, suggesting a well-defined sample Fermi edge and that the Fermi level is intersecting the upper VB states. Therefore, we conclude that our sample is a p-type semiconductor.

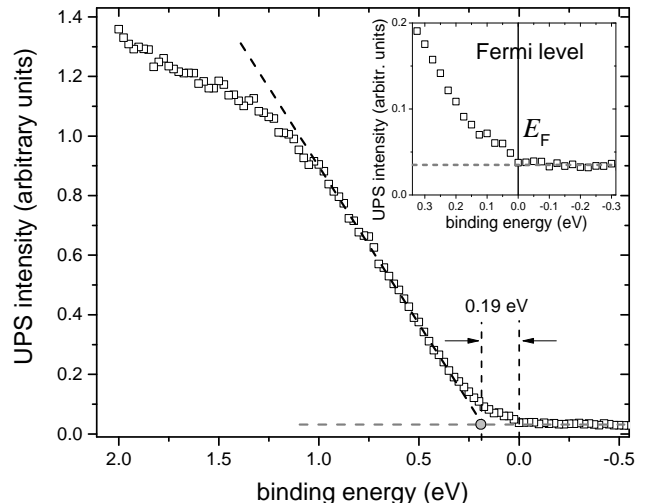


FIG. 5. UPS data covering the VBM region measured with a photon energy $\hbar\omega = 21.2$ eV. The position of the VBM at 0.19 eV is estimated by the leading edge method (see text). In the inset the signal intensity around $E = 0$ (analyzer Fermi edge) is shown in detail.

III. MAGNETIZATION MEASUREMENTS

In order to determine the Néel temperature T_N on NaMnAs single crystals, we have performed high temperature magnetization measurements using VSM Oven option (Quantum Design PPMS). A set of about 15 single crystals, with total mass of 16 mg was placed in the sample holder and fixed by copper foil with magnetic field oriented in the basal plane (see Supplemental Material). The temperature dependence of magnetization was measured in the range 300-880 K and magnetic field of 1 T.

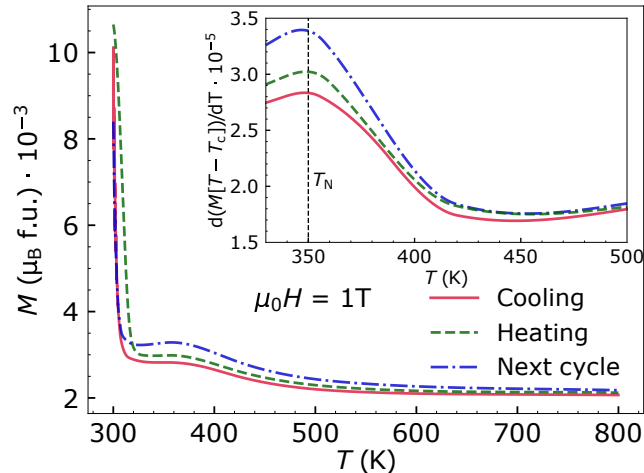


FIG. 6. Susceptibility measurements (temperature dependent magnetisation at $B = 1$ T). The shift of maximum in the inset, upon thermal cycling, is likely an artefact of the signal-enhancement method.

We have observed, that the overall magnetic signal increases and slowly saturates upon repeating the heating cycles (Fig. 6). This is probably due to the fact, that in vacuum and high temperatures conditions, the sample surface becomes Na deficient and larger amount of MnAs phase is grown, increasing the paramagnetic signal. This hypothesis is supported by XRD measurements of as grown and annealed piece of crystal (see Supplemental Material), where new MnAs peaks appeared after annealing the crystal at similar conditions. MnAs in its hexagonal form order ferromagnetically at around 315 K with magnetic-field dependent temperature hysteresis [51–53].

Magnetization isotherm plots (see Fig. 7) at 400, and 600 K show linear behavior without hysteresis, while the isotherm at 350 K shows a weak paramagnetic contribution and a weak up-turn at high magnetic fields. At lower temperatures (not shown) a hysteresis can be seen connected to the presence of FM impurity of MnAs.

Considering the presence of MnAs impurities, the magnetization measurement should be considered as partially qualitative. The value of T_N fits, however, in the expected range between 295 a 643 K reported by Bronger

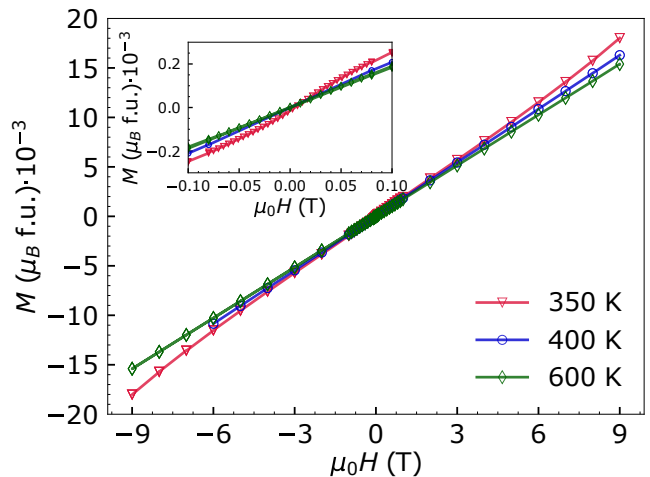


FIG. 7. Magnetization isotherm of NaMnAs single crystals with magnetic field oriented in basal plane.

et al. [37].

IV. MAGNETIC ORDER

Results of the previous Section confirm NaMnAs as an antiferromagnetic material. Contrary to the simple case of ferromagnets, this however still allows for many types of magnetic order described by the set of Mn magnetic moments $\{S_{\text{Mn}}\vec{m}_i\}$ where we assume $|\vec{m}_i| = 1$ and equal magnitude of all Mn moments S_{Mn} . From theoretical point of view, the ground state follows from energy minimisation of

$$E = -\frac{1}{2} S_{\text{Mn}}^2 \sum_{ij} J_{ij} \vec{m}_i \cdot \vec{m}_j \quad (1)$$

once we neglect higher order terms (as discussed in Appendix). While we relegate a quantitative discussion of the Heisenberg parameters J_{ij} to Sec. VI.B, we now qualitatively describe the implications of this form of energy on the ordering of classical magnetic moments \vec{m}_i arranged on lattice shown in Fig. 3. To begin with, let us assume that non-zero J_{ij} occur only for nearest neighbours in the basal plane (intralayer coupling J_0) and along the c -axis (interlayer coupling J_c). In terms of signs, there are then four options, one leading to ferromagnetic order (when both J_0, J_c are positive) and the three remaining options forcing three different types of AFM order. For $J_0 > 0$ and $J_c < 0$, each Mn layer is ferromagnetically ordered and such AFM structure has never been identified across AMnX compounds (where A is an alkali metal and X is As or Sb) as the early neutron scattering measurements by Bronger et al.[37] revealed. The remaining two options with $J_0 < 0$ lead to a checkerboard pattern of moments, interleaved along the $+z$ or $-z$ out-of-plane direction with propagation vector either $\vec{k} = (000)$ or $(00\frac{1}{2})$. Bronger et al. also determined

$S_{\text{Mn}} = 3.45$ at room temperature in NaMnAs; it was not clear however, at which temperature the magnetic order collapses (the only piece of information to this end was that at 643 K, magnetic signal in neutron scattering data has already vanished).

While for $A=\text{Li}$ or K the Mn planes are however further coupled with Heisenberg exchange parameters favoring anti-parallel couplings along the (001) axis, effectively resulting in a twice as big magnetic unit cell, in NaMnAs the manganese layers are only weakly coupled to favor a parallel ordering: in other words, $J_c > 0$ should apply this case. Such simplified qualitative consideration can become inappropriate when J_{ij} in Eq. (1) do not decay fast enough with the distance between sites i and j but in case of NaMnAs, as we show in Sec. VI.B, the effective magnetic interactions are rather short-ranged.

We conclude this short Section by several remarks on theoretical studies in this class of materials. Zhou et al. [38] compared the ground state energy within density functional theory (DFT) framework and the energetically most favourable magnetic order is the one shown in Fig. 3. We confirm this also for DFT+U (as used previously [31] for LiMnAs and KMnAs; see also Sec. VI.A) whereas the energy cost of doubled magnetic unit cell is at the level of few meV per f.u.

V. MEASUREMENTS OF THE OPTICAL GAP

Optical transmission measurements offer a straightforward means to prove the presence of a band gap. The measurements were performed using Woollam RC2 Mueller matrix ellipsometer in the spectral range from 0.7 to 6 eV. The data were corrected for the baseline measurement without the sample in optical path, the resulting transmission data is shown in Fig. 8 on a logarithmic scale, with the raw data in the inset. The higher level of noise above 1.2 eV is due to extremely low transmission where the detected light intensity is reaching the sensitivity limit of the equipment. A rapid decrease of transmission towards higher energies near 1 eV is a notable sign of the onset of interband transitions, giving the approximate estimation of the gap.

Given the definition of $T(E) = I/I_0$, a ratio of incoming and outgoing intensity of light at energy $E = \hbar\omega$, in terms of absorption coefficient α , the sample width w , the imaginary part of complex permittivity $\epsilon = \epsilon_1 + i\epsilon_2$ can easily be extracted from Fig. 8. We write

$$-\ln T(E) = w \frac{E}{\hbar c} \cdot \frac{\epsilon_2}{\sqrt{\epsilon_1}}$$

and fit the experimental data assuming $\epsilon_2 \propto \sqrt{E - E_0}$ for a direct and $\epsilon_2 \propto (E - E_0)^2$ for an indirect gap. The measurement clearly indicates that there is a band gap: an indirect (direct) band gap fit assuming $\epsilon_1 = \text{const.}$ yields the gap of 0.9 (1.16) eV. The absorption shoulder at lower energies may be ascribed to defect states inside the gap or twisting of the planes with respect to each

other. As already discussed above, although the symmetric XRD scan presented in Fig. 1 suggest high quality of single crystal, the single crystal diffraction showing the full reciprocal space shows on significant basal plane mosaicity, which can be source of the low-temperature absorption shoulder. Another methods, such as spectroscopic ellipsometry can provide wider information about the absorption edge and band structure of the material and will be subject of our further studies of NaMnAs.

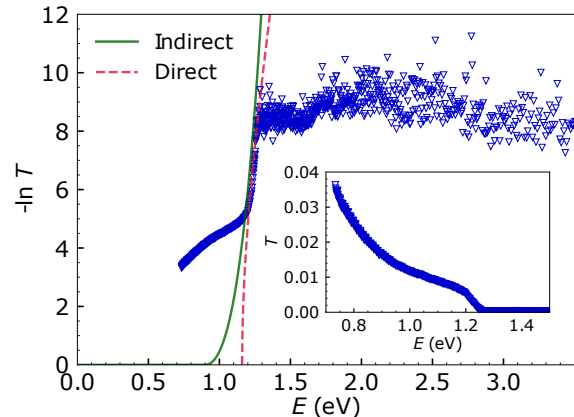


FIG. 8. *Inset:* The spectral dependence of the optical transmission T . *Main plot:* The same data replotted as $-\ln T(E)$; fits in the interval 1.2 - 1.4 eV by direct (red, dashed) or indirect band gap model allow to estimate the band gap.

VI. THEORETICAL MODELLING

A. Electronic structure

Magnetic compounds containing manganese in the nominal $3d^5$ configuration often share a generic electronic structure: while the existence of the gap is optional, the anion-based bands provide a background for the spin-split Mn d -states one of which is below and the other above Fermi level. Previous ab initio calculations [31, 38] predicted that tetragonal XMnAs antiferromagnetic materials (where X is an alkali metal) do have a gap and, for example, CuMnAs is a metal with low density of states (DOS) at the Fermi level (E_F), see Fig. 3 in Ref. [24]. Size of the gap obtained by ab initio methods can be problematic and density functional theory (DFT) calculations are known to often give too small gaps even in simple systems (as opposed to strongly correlated ones) such as GaAs.

We chose local density approximations (LDA) as our starting point for DFT. Apart from an undersized gap, a simple LDA calculation leads to Mn magnetic moments about 10% smaller than what is found experimentally. Regardless of the detailed implementation of DFT+U, magnetic moments become larger when U increases, as a consequence of the larger separation in energy of the ma-

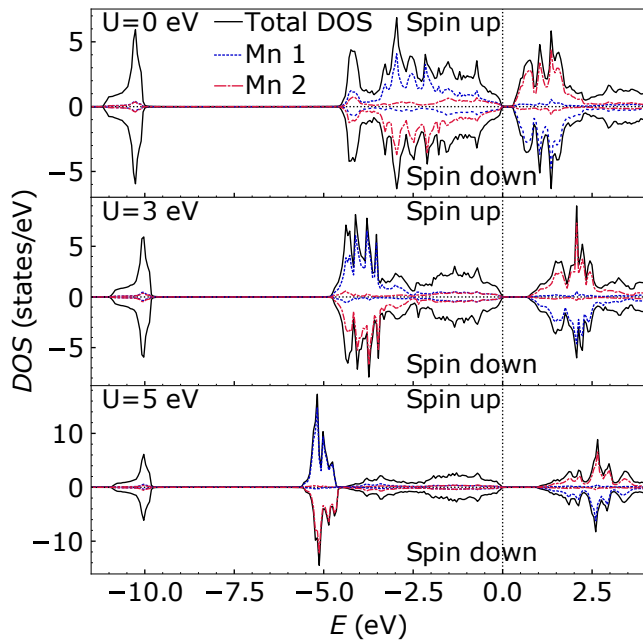


FIG. 9. Total and Mn-projected DOS from LDA+U calculations with $U = 0, 3, 5$ eV.

majority and minority Mn d -states. Symptoms of such gradual changes can be seen in the density of states (DOS) shown in Fig. 9. A compromise among several factors (magnetic moments, gap size, estimates of Néel temperature discussed in the next subsection) directed us to a value of U around 5 eV. On the experimental side, realistic magnitude of Mn magnetic moments [37] would suggest somewhat smaller U but the final judgement should depend on a more direct quantity (such as Mn d -peak characteristics in UPS). In the following, we use both LDA and LDA+U in the atomic sphere approximation (ASA) as implemented within the spin-polarized relativistic Korringa-Kohn-Rostoker (SPRKKR) electronic structure package [54] and cross-check the results using generalised gradient approximation to DFT in linearised augmented-plane-wave (LAPW) method in another package [55]. The latter yield an out-of-plane magnetic anisotropy around 0.2 meV per formula unit free of any strong dependence on the value of U with a modest correction due to dipolar interactions. This is somewhat larger than in CuMnAs (see App. A of Ref. 56).

B. Heisenberg parameters

Effective spin Hamiltonians allow to study finite-temperature properties of magnetic systems (such as NaMnAs) at a reasonable computational cost (see also discussion in Appendix). Depending on their complexity, they use various parameters as input where Heisenberg exchange parameters J_{ij} play the central role. In our work, J_{ij} are determined using the method of Ref. 57 i.e.

starting from the perturbed (by δV_i , see Appendix) antiferromagnetic ground state (reflected in the T -matrices) and evaluating

$$J_{ij} = \frac{1}{4\pi} \int_{-\infty}^{E_F} dE \text{Im Tr } \delta V_i T_{\uparrow}^{ij} \delta V_j T_{\downarrow}^{ji} \quad (2)$$

Herewith, the complicated quantum-mechanical problem (crystal with many electrons, for example) is mapped to a relatively simple lattice model of classical spins with pair interactions only. In this model, total energy (more precisely, its part — see Appendix) of the system is approximated by Eq. (1) and using a Monte Carlo simulation, various thermodynamic quantities can be estimated. For example, temperature-dependent sublattice magnetisation can be extrapolated to zero and thus Néel temperature obtained.

In Fig. 10, we show Heisenberg parameters obtained from an LDA+U zero-temperature calculation ($U = 5$ eV) plotted as a function of the distance between individual Mn atoms. This is a simplified representation of the situation created by an anisotropic crystal: the complete layout of J_{ij} 's in real space is shown in the Appendix. It should be pointed out that the couplings are clearly dominated by the nearest-neighbour (NN) pairs within one plane of Mn atoms (both inter- and intra-sublattice) and the next-nearest-neighbour J_{ij} are more than an order of magnitude smaller. The antiferromagnetic inter-sublattice NN coupling (corresponding to $J_0 < 0$ in terms of the discussion in Sec. IV) is further augmented by *ferromagnetic* intra-sublattice NN interaction. More distant pairs interact feebly and coupling between different layers is also weak. The NN in a different layer, i.e. shortest inter-layer coupling (corresponding to J_c and highlighted by an arrow in Fig. 10) belongs to the same magnetic sublattice and $|J_c/J_0| \sim 10^{-2}$.

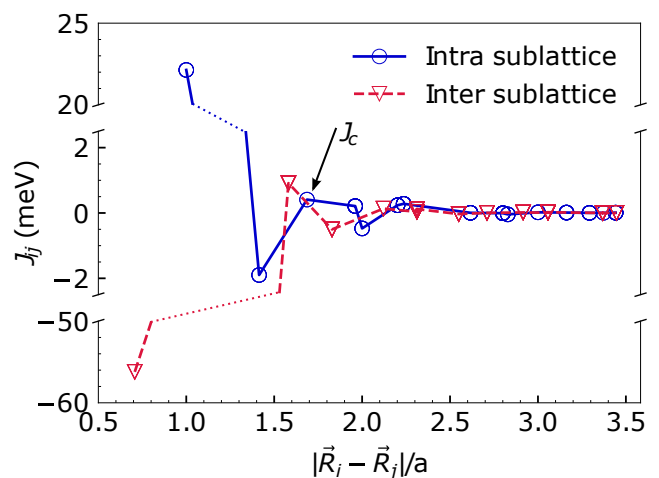


FIG. 10. Calculated Heisenberg exchange parameters J_{ij} plotted as a function of distance between sites i, j . The arrow indicates J_{ij} corresponding to the leading coupling between layers (J_c in the qualitative discussion of Sec. IV).

Comparing LDA to LDA+U calculations, we find that the coupling between Mn magnetic moments decreases with increasing U . However, this seems to be compensated by the enhancement of magnetic moments (see the discussion of Monte Carlo simulations in the next Subsection). Zhou et al.[38] noted that calculations are robust with respect to the alternative choice of GGA rather than LSDA exchange-correlation functional, thanks to the over-binding artefact of the latter cancelling out in taking the difference. The reduced dimensionality of the magnetic interactions, mainly confined to the (001) Mn planes, can explain the much smaller ordering temperature revealed by experiments and by Monte Carlo simulation, as opposed to cruder early estimates in terms of total energy difference alone, or mean-field theory calculations.

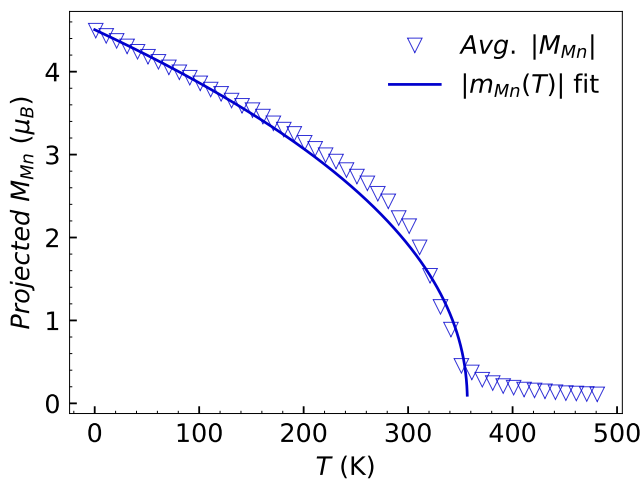


FIG. 11. Mn-resolved average spin magnetic moment (blue triangles) vs. temperature, from Monte Carlo simulations (see text).

C. Néel temperature

Several approaches to estimating theoretically the ordering temperature are possible and their short review is given in Appendix. Here, we employ Monte Carlo (MC) calculations[58] as implemented the Uppsala Atomistic Spin Dynamics UppASD code [59]. Their input are the Heisenberg parameters discussed in the previous subsection.

The lower T_N of NaMnAs with respect to CuMnAs can be tentatively understood as a consequence of different effective coordination, or local environment, for the Mn atoms within the two materials. While for manganese pnictide CuMnAs the transition metal (Mn atoms) is arranged in a rumpled geometry (2c positions in the CuSb₂-type structure), in NaMnAs the manganese cre-

ates flat planes (2a positions of the CuSb₂ type structure). In combination with the fairly short-ranged J_{ij} s which present only weak coupling across such planes, the magnetic Hamiltonian becomes effectively 2D.

Temperature-dependent sublattice magnetisation for NaMnAs shown in Fig. 11 suggests that ordering temperature is slightly above 350 K. This agrees well with experimental data in Fig. 6.

VII. CONCLUSIONS

We have prepared the room temperature antiferromagnet NaMnAs for the first time in the single crystalline form. The single crystals have layered tetragonal structure and can be easily cleaved within the basal plane, the single crystals are in general very soft. The magnetization measurement showed the Néel temperature to be 350 K being in agreement with the temperature ranged defined by previous neutron diffraction experiments on polycrystals [37]. Using Ultraviolet photoemission spectroscopy and optical transmittivity measurements we showed that NaMnAs is a p-type semiconductor with a band gap between 0.9 and 1.16 eV depending on whether the band gap is direct or indirect, respectively. The detail studies of the type of band gap and band structure in general will be subject of our further work. In conclusion NaMnAs has been found to be a new room temperature antiferromagnetic semiconductor, together with the layered structure it can be promising material for fabrication of functional devices. However, further studies of basic physical properties and possibilities to modify its electronic properties e.g. by chemical substitutions of formation of multi layers has to be done prior to looking into application sphere.

ACKNOWLEDGEMENTS

We gratefully acknowledge computational resources from the Information Technology for Innovation (IT4I) grants: OPEN-19-45, OPEN-20-12 and from the project "e-Infrastruktura CZ" (e-INFRA LM2018140) provided within the program Projects of Large Research, Development and Innovations Infrastructures, Operational Program Research, Development and Education financed by European Structural and Investment Funds and the Czech Ministry of Education, Youth and Sports (Project MATFUN - CZ.02.1.01/0.0/0.0/15_003/0000487). Single crystals growth and characterization was performed in MGML (mgml.eu), which is supported within the program of Czech Research Infrastructures (project no. LM2018096). M.V. and J.H. acknowledge support from the Czech Ministry of Education, Youth and Sports (Project No. SOLID21-CZ.02.1.01/0.0/0.0/16_019/0000760). J.M. acknowledges support from GAČR Project No. 2018725S.

- [1] T. Jungwirth, J. Wunderlich, V. Novák, K. Olejník, B. L. Gallagher, R. P. Champion, K. W. Edmonds, A. W. Rushforth, A. J. Ferguson, and P. Nemeč, *Rev. Mod. Phys.* **86**, 855 (2014).
- [2] X. Marti, I. Fina, and T. Jungwirth, *IEEE Trans. Magn.* **51**, 5 (2015).
- [3] O. Gomonay, T. Jungwirth, and J. Sinova, *Phys. Status Solidi - Rapid Res. Lett.* **11**, 1 (2017), arXiv:1701.06556.
- [4] M. B. Jungfleisch, W. Zhang, and A. Hoffmann, *Phys. Lett. Sect. A Gen. At. Solid State Phys.* **382**, 865 (2018).
- [5] X. Marti, I. Fina, C. Frontera, J. Liu, P. Wadley, Q. He, R. Paull, J. Clarkson, J. Kudrnovský, I. Turek, J. Kuneš, D. Yi, J.-H. Chu, C. Nelson, L. You, E. Arenholz, S. Salahuddin, J. Fontcuberta, T. Jungwirth, and R. Ramesh, *Nat. Mater.* **13**, 367 (2014).
- [6] K. Olejník, V. Schuler, X. Marti, V. Novák, Z. Kašpar, P. Wadley, R. P. Champion, K. W. Edmonds, B. L. Gallagher, J. Garces, M. Baumgartner, P. Gambardella, and T. Jungwirth, *Nat. Commun.* **8**, 15434 (2017).
- [7] P. Wadley, S. Reimers, M. J. Grzybowski, C. Andrews, M. Wang, J. S. Chauhan, B. L. Gallagher, R. P. Champion, K. W. Edmonds, S. S. Dhesi, F. Maccherozzi, V. Novak, J. Wunderlich, and T. Jungwirth, *Nat. Nanotechnol.* **13**, 362 (2018), arXiv:1711.05146.
- [8] S. M. Rezende, A. Azevedo, and R. L. Rodríguez-Suárez, *J. Appl. Phys.* **126**, 151101 (2019).
- [9] V. Kruglyak, O. Demokritov, and D. Grundler, *J. Phys. D. Appl. Phys.* **43**, 250301 (2010).
- [10] D. Grundler, *J. Phys. D. Appl. Phys.* **49**, 391002 (2016).
- [11] A. V. Chumak and H. Schultheiss, *J. Phys. D. Appl. Phys.* **50**, 300201 (2017).
- [12] D. Ghader and A. Khater, *Sci. Rep.* **9**, 1 (2019).
- [13] A. Ross, R. Lebrun, O. Gomonay, D. A. Grave, A. Kay, L. Baldtrati, S. Becker, A. Qaiumzadeh, C. Ulloa, G. Jakob, F. Kronast, J. Sinova, R. Duine, A. Brataas, A. Rothschild, and M. Kläui, *Nano Lett.* **20**, 306 (2019).
- [14] J. Han, P. Zhang, Z. Bi, Y. Fan, T. S. Safi, J. Xiang, J. Finley, L. Fu, R. Cheng, and L. Liu, *Nat. Nanotechnol.* 10.1038/s41565-020-0703-8 (2020).
- [15] V. Baltz, A. Manchon, M. Tsoi, T. Moriyama, T. Ono, and Y. Tserkovnyak, *Reviews of Modern Physics* **90**, 15005 (2018), arXiv:1606.04284.
- [16] T. Jungwirth, J. Sinova, A. Manchon, X. Marti, J. Wunderlich, and C. Felser, *Nat. Phys.* **14**, 200 (2018).
- [17] P. Wadley, B. Howells, J. Zelezny, C. Andrews, V. Hills, R. Champion, V. Novak, K. Olejnik, F. Maccherozzi, S. Dhesi, S. Martin, T. Wagner, J. Wunderlich, F. Freimuth, Y. Mokrousov, J. Kune, J. Chauhan, M. Grzybowski, A. Rushforth, K. Edmonds, B. Gallagher, and T. Jungwirth, *Science (80-.)*. **351**, 587 (2016).
- [18] M. J. Grzybowski, P. Wadley, K. W. Edmonds, R. Beardley, V. Hills, R. P. Champion, B. L. Gallagher, J. S. Chauhan, V. Novak, T. Jungwirth, F. Maccherozzi, and S. S. Dhesi, *Phys. Rev. Lett.* **118**, 1 (2017).
- [19] P. Wadley and K. W. Edmonds, *Chinese Phys. B* **27**, 10.1088/1674-1056/27/10/107201 (2018).
- [20] Z. Kašpar, M. Surýnek, J. Zubáč, F. Krizek, V. Novák, R. P. Champion, M. S. Wörnle, P. Gambardella, X. Marti, P. Němec, K. W. Edmonds, S. Reimers, O. J. Amin, F. Maccherozzi, S. S. Dhesi, P. Wadley, J. Wunderlich, K. Olejník, and T. Jungwirth, arXiv Prepr. , 1909.09071v2 (2019), arXiv:1909.09071.
- [21] F. MácA, J. Mašek, O. Stelmakhovych, X. Martí, H. Reichlová, K. Uhlřřová, P. Beran, P. Wadley, V. Novák, and T. Jungwirth, *Journal of Magnetism and Magnetic Materials* **324**, 1606 (2012).
- [22] P. Wadley, V. Hills, M. Shahedkhal, K. Edmonds, R. Champion, V. Novák, B. Ouladdiaf, D. Khalyavin, S. Langridge, V. Saidl, P. Nemeč, A. Rushforth, B. Gallagher, S. Dhesi, F. Maccherozzi, J. Železný, and T. Jungwirth, *Sci. Rep.* **5**, 17079 (2015).
- [23] F. MácA, J. Kudrnovský, V. Drchal, K. Carva, P. BaláŽ, and I. Turek, *Phys. Rev. B* **96**, 094406 (2017).
- [24] M. Veis, J. Minár, G. Steciuk, L. Palatinus, C. Rinaldi, M. Cantoni, D. Kriegner, K. K. Tikuišis, J. Hamrle, M. Zahradník, R. Antoš, J. Železný, L. Šmejkal, X. Marti, P. Wadley, R. P. Champion, C. Frontera, K. Uhlřřová, T. Duchoň, P. Kužel, V. Novák, T. Jungwirth, and K. Výborný, *Phys. Rev. B* **97**, 2 (2018).
- [25] F. MácA, J. Kudrnovský, P. BaláŽ, V. Drchal, K. Carva, and I. Turek, *J. Magn. Magn. Mater.* **474**, 467 (2019).
- [26] K. Uhlřřová, E. Duverger-Nédellec, R. H. Colman, J. Volný, B. Vondráčková, and K. Carva, *J. Alloys Compd.* **771**, 680 (2018).
- [27] A. A. Sapozhnik, M. Filianina, S. Y. Bodnar, A. Lami-rand, M. A. Mawass, Y. Skourski, H. J. Elmers, H. Zabel, M. Kläui, and M. Jourdan, *Phys. Rev. B* **97**, 134429 (2018), arXiv:1803.03022.
- [28] M. Odashima, A. Marmodoro, P. Buczek, A. Ernst, and L. Sandratskii, *Phys. Rev. B* **87**, 174420 (2013).
- [29] Y. Kajiwara, K. Harii, S. Takahashi, J. Ohe, K. Uchida, M. Mizuguchi, H. Umezawa, H. Kawai, K. Ando, K. Takanashi, S. Maekawa, and E. Saitoh, *Nature* **464**, 262 (2010).
- [30] L. J. Cornelissen, J. Liu, R. a. Duine, J. B. Youssef, and B. J. van Wees, *Nat. Phys.* , 1 (2015).
- [31] T. Jungwirth, V. Novák, X. Martí, M. Cukr, F. MácA, A. B. Shick, J. Mašek, P. Horodyská, P. Němec, V. Holý, J. Zemek, P. Kužel, I. Němec, B. L. Gallagher, R. P. Champion, C. T. Foxon, and J. Wunderlich, *Phys. Rev. B* **83**, 035321 (2011).
- [32] P. Wadley, V. Novák, R. P. Champion, C. Rinaldi, X. Martí, H. Reichlová, J. Železný, J. Gazquez, M. A. Roldan, M. Varela, D. Khalyavin, S. Langridge, D. Kriegner, F. MácA, J. Mašek, R. Bertacco, V. Holý, A. W. Rushforth, K. W. Edmonds, B. L. Gallagher, C. T. Foxon, J. Wunderlich, and T. Jungwirth, *Nature Communications* **4**, 2322 (2013), arXiv:1402.3624.
- [33] V. Hills, P. Wadley, R. P. Champion, V. Novak, R. Beardley, K. W. Edmonds, B. L. Gallagher, B. Ouladdiaf, and T. Jungwirth, *J. Appl. Phys.* **117**, 172608 (2015).
- [34] L. Linowski and W. Bronger, *ZAAC - J. Inorg. Gen. Chem.* **409**, 221 (1974).
- [35] H.-U. Schuster and G. Achenbach, *Zeitschrift für Naturforsch. B* **33**, 113 (1978).
- [36] G. Achenbach and H. Schuster, *Z.Anorg.allg.Chem.* **475**, 9 (1981).
- [37] W. Bronger, P. Müller, R. Höppner, and H. Schuster, *ZAAC - J. Inorg. Gen. Chem.* **539**, 175 (1986).
- [38] W. Zhou, S. Wu, and S. Li, *J. Magn. Magn. Mater.* **420**, 19 (2016).

- [39] A. Beleanu, J. Kiss, G. Kreiner, C. Köhler, L. MÜchler, W. Schnelle, U. Burkhardt, S. Chadov, S. Medvediev, D. Ebke, C. Felser, G. Cordier, B. Albert, A. Hoser, F. Bernardi, T. I. Larkin, D. Pröpper, A. V. Boris, and B. Keimer, *Phys. Rev. B* **88**, 184429 (2013).
- [40] A. Beleanu, *Ternary Lithium Based Compounds used for Technological Applications*, Ph.D. thesis, Mainz University (2014).
- [41] J. Yang, A. Wegner, C. M. Brown, and D. Louca, *Appl. Phys. Lett.* **122**105, 122105 (2018).
- [42] A. Wegner, D. Louca, K. M. Taddei, and J. Neuefeind, *Phys. Rev. B* **102**, 020403 (2020).
- [43] K. Uhlřřova, R. Tarasenko, F. J. Martınez-Casado, B. Vondračkova, and Z. Matěj, *Journal of Alloys and Compounds* **650**, 224 (2015).
- [44] B. a. o. a. Nesbitt, *American mineralogist* (1998).
- [45] R. Tarasenko, M. Vališka, M. Vondraček, K. Horakova, V. Tkac, K. Carva, P. Balaz, V. Holy, G. Springholz, V. Sechovsky, and J. Honolka, *Physica B: Condensed Matter* **481**, 262 (2016).
- [46] M. Taguchi, T. Uozumi, and A. Kotani, *Journal of the Physical Society of Japan* **66**, 247 (1997), <https://doi.org/10.1143/JPSJ.66.247>.
- [47] P. Wernet, B. Sonntag, M. Martins, P. Glatzel, B. Obst, and P. Zimmermann, *Phys. Rev. A* **63**, 050702 (2001).
- [48] A. Hariki, T. Uozumi, and J. Kuneš, *Phys. Rev. B* **96**, 045111 (2017).
- [49] L. Zhong Zhao and V. Young, *Journal of Electron Spectroscopy and Related Phenomena* **34**, 45 (1984).
- [50] E. A. Kraut, R. W. Grant, J. R. Waldrop, and S. P. Kowalczyk, *Phys. Rev. Lett.* **44**, 1620 (1980).
- [51] Y. Koshkid'ko, E. Dilmieva, J. Cwik, K. Rogacki, D. Kowalska, A. Kamantsev, V. Koledov, A. Mashirov, V. Shavrov, V. Valkov, A. Golovchan, A. Sivachenko, S. Shevyrtalov, V. Rodionova, I. Shchetinin, and V. Sampath, *Journal of Alloys and Compounds* **798**, 810 (2019).
- [52] A. de Campos, M. Mota, S. Gama, A. Coelho, B. White, M. da Luz, and J. Neumeier, *Journal of Crystal Growth* **333**, 54–58 (2011).
- [53] A. Carvalho, A. Coelho, S. Gama, F. Gandra, P. Ranke, and N. De Oliveira, *The European Physical Journal B - Condensed Matter and Complex Systems* **78**, 137 (2010).
- [54] H. Ebert, D. Ködderitzsch, and J. Minar, *Reports Prog. Phys.* **74**, 096501 (2011).
- [55] P. Blaha, K. Schwarz, F. Tran, R. Laskowski, G. K. H. Madsen, and L. D. Marks, *The Journal of Chemical Physics* **152**, 074101 (2020), <https://doi.org/10.1063/1.5143061>.
- [56] J. Volny, D. Wagenknecht, J. Zelezny, P. Harcuba, E. Duverger-Nedellec, R. H. Colman, J. Kudrnovsky, I. Turek, K. Uhlřřova, and K. Vyborny, *Arxiv*, 1 (2020), arXiv:2001.01947.
- [57] A. I. Liechtenstein, M. I. Katsnelson, and V. A. Gubanov, *Journal of Physics F: Metal Physics* **14**, L125 (1984).
- [58] O. Eriksson, A. Bergman, L. Bergqvist, and J. Hellsvik, *Atomistic Spin-Dynamics*, first edit ed. (Oxford University Press, Uppsala, 2017) arXiv:arXiv:1011.1669v3.
- [59] J. Hellsvik, D. Thonig, K. Modin, D. Iușan, A. Bergman, O. Eriksson, L. Bergqvist, and A. Delin, *Phys. Rev. B* **99**, 104302 (2019), arXiv:1804.03119.